Erosion–corrosion behavior of X65 carbon steel in oilfield formation water

Jingbo Liu[1, 2]，Jihui Wang[1, 2,*], Wenbin Hu[2]

[1]State Key Laboratory of Hydraulic Engineering Simulation and Safety, Tianjin University, Tianjin 300350, P R China
[2]Tianjin Key Laboratory of Composite and Functional Materials, School of Materials Science and Engineering, Tianjin University, Tianjin 300350, P R China
[*]E-mail: jhwang@tju.edu.cn

Erosion–corrosion behavior of an X65 steel reducer in oilfield formation water containing quartz sand particles was investigated using circulating loop system and scanning electron microscopy (SEM). The corrosion behavior of the X65 reducer during the erosion–corrosion was determined by electrochemical impedance spectroscopy (EIS), and the erosion behavior of the X65 reducer was simulated and calculated via computational fluid dynamic (CFD) method. By the synergistic interaction between erosion and corrosion, the pure corrosion rate, pure erosion rate, corrosion-enhanced erosion rate and erosion-enhanced corrosion rate of the typical reducer locations in the erosion–corrosion rate were quantified and compared. The experimental and simulation results indicated that with the decreasing of tube diameter the erosion–corrosion rate, erosion rate (total erosion rate, pure erosion rate and corrosion-enhanced erosion rate) and their percentages in erosion–corrosion rate are increased. And the total corrosion rate and erosion-enhanced corrosion rate are also increased with the decreasing of tube diameter, but their percentages in erosion–corrosion rate are reduced. From the location of tube top, tube side to the tube bottom, a similar erosion–corrosion behavior could be obtained except for the reduction of corrosion-enhanced erosion rate and its percentage in erosion–corrosion rate. This erosion–corrosion behavior of the reducer is result from the distribution of flow velocity and sand particle concentration and the synergistic interaction between erosion and corrosion, especially the erosion-enhanced corrosion behavior.

1. INTRODUCTION

Erosion–corrosion normally occurs under flow induced corrosion process, in which there is an obvious synergistic interaction between mechanical erosion and electrochemical corrosion [1, 2].

Erosion–corrosion problems are widely encountered in the petroleum, chemical, marine, transportation, hydropower and other industries at sudden changes in the flow system geometry such as bends, pumps, valves and propellers, by which serious accidents and damage of material or component could be arisen [3-5].

According to the type of medium, the erosion–corrosion can be divided into three types: single-phase flow, two-phase flow and multi-phase flow erosion–corrosion. Two-phase flow erosion–corrosion is the most common one with a wide industrial background, which is the focus of research [6, 7]. Erosion–corrosion is not simply the sum of erosion and corrosion [8, 9]. The total loss of metallic materials caused by liquid–solid two-phase flow erosion–corrosion is related to pure corrosion weight loss and pure erosion weight loss, and to the synergy between mechanical effects caused by particle impact and corrosion [10-13]. In general, the erosion–corrosion rate of steel comprises four parts: pure corrosion rate, pure erosion rate, corrosion-enhanced erosion rate and erosion-enhanced corrosion rate [14-16]. Previous research efforts only investigated the variation of total erosion–corrosion rate, and few studies are available on the synergistic effect of corrosion and erosion. So far, many countries have carried out simulation studies and software development for erosion [17]. Computational fluid dynamics (CFD) can help determine flow velocity in complex pipelines, as well as near-wall turbulence intensity, which is important for predicting erosion-sensitive areas [18, 19]. Various fluid field parameters under liquid–solid two-phase flow conditions were numerically simulated by many researchers [20, 21].

Typical pipe fittings such as reducer, elbow, and tee are the most susceptible to erosion–corrosion failure. The erosion–corrosion of elbow and tee tubes has been studied by many researchers [14, 22, 23]. However, few studies are available on reducers. The reducer, which can change the pipe diameter to adjust the medium flow velocity and smoothen the flow line, is a commonly used connection fitting in oil and gas transportation systems. However, a sudden change of pipe diameter would cause significant differences in erosion–corrosion behavior at different positions of the reducer. The changes that would happen to these four components of erosion–corrosion rate with the change of the diameter of the reducer have not been elucidated.

In this work, a circulating loop system was developed to study erosion–corrosion behavior of X65 steel reducer in the formation water of oil field containing quartz sand particles. Weight loss and electrochemical impedance spectroscopy (EIS) measurements were applied to quantify the four components of the total erosion–corrosion rate at the different positions of reducer. The corroded morphologies before and after removing corrosion products were observed using scanning electron microscope (SEM). Furthermore, the flow pattern and damage pattern within reducer were characterized by computational fluid dynamics (CFD) simulation.

2. EXPERIMENTAL AND CFD SIMULATION

2.1. Materials and experimental solution

The electrode material used for the erosion–corrosion test was X65 pipeline carbon steel. The chemical composition (mass fraction) of the X65 steel was C 0.09%, Mn 1.3%, Si 0.26%, Ni 0.15%, Mo 0.17%, Cr 0.04% and Fe balance. The exposed area of all electrode (A0º, A90º, A180º, A270º, B0º, B90º, B180º, B270º, C0º, C90º, C180º, C270º) samples was 6 mm×5 mm. One copper wire was connected to

the back of each electrode for electrochemical measurement. Before erosion–corrosion tests, all electrode surfaces were subsequently abraded with 800, 1200 and 2000 grit silicon carbide paper, cleared with deionized water, and then degreased in ethanol.

The composition of oilfield formation water is shown in Table 1 [14]. The pH value of the test solution was 6.7. Quartz sand particles with size of 250-400 μm were utilized in this test with a load of 1 wt%.

Table 1. Solution composition of oilfield formation water (g/L).

Composition	NaCl	KCl	CaCl$_2$	Na$_2$SO$_4$	MgCl$_2 \cdot 6H_2O$	NaHCO$_3$
Content	90.44	2.20	17.32	0.43	6.33	0.49

2.2. Erosion–corrosion test

A circulating loop system was designed and used to perform erosion–corrosion experiments, as shown in Fig. 1. This loop system is composed by water tank, screw pump, flowmeter, stirrer, pipes and electrode test section. The inner diameters of inlet straight pipe and outlet straight pipe were 30 mm and 18 mm respectively. The distance between inlet straight pipe and outlet straight pipe was 16.5 mm. All electrodes were sealed in the grooves of reducer with silicone. Electrode position diagram of the reducer is shown in Fig. 2. There are four specimens in the inlet straight pipe (electrode A0º, A90º, A180º, A270º), four specimens at the reducer section (electrode B0º, B90º, B180º, B270º), four specimens in the outlet straight pipe (electrode C0º, C90º, C180º, C270º) (Fig. 2c).

Erosion–corrosion tests were carried out in a flow velocity of 0.5 m/s at the temperature of 26℃. The erosion–corrosion testing was conducted continuously for 12 h. After erosion–corrosion tests, the specimens were degreased, rinsed, dried and weighted to obtain the total erosion–corrosion rate (V_T). The accuracy of analytical balance was 0.01mg.

After erosion–corrosion experiments, the surface morphologies of representative electrodes before and after removing corrosion products were obtained by scanning electron microscopy (SEM).
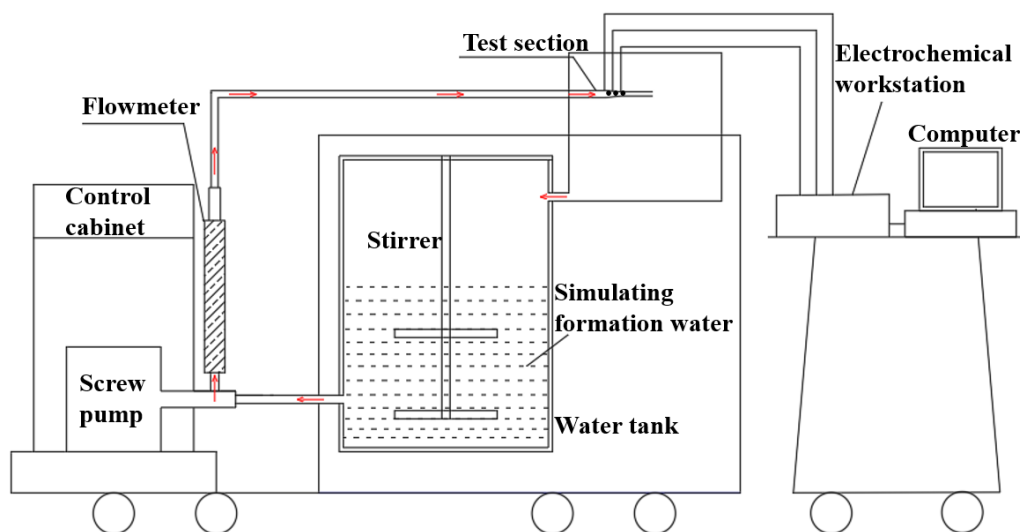

Figure 1. Schematic diagram of self-designed erosion–corrosion circulating loop system.
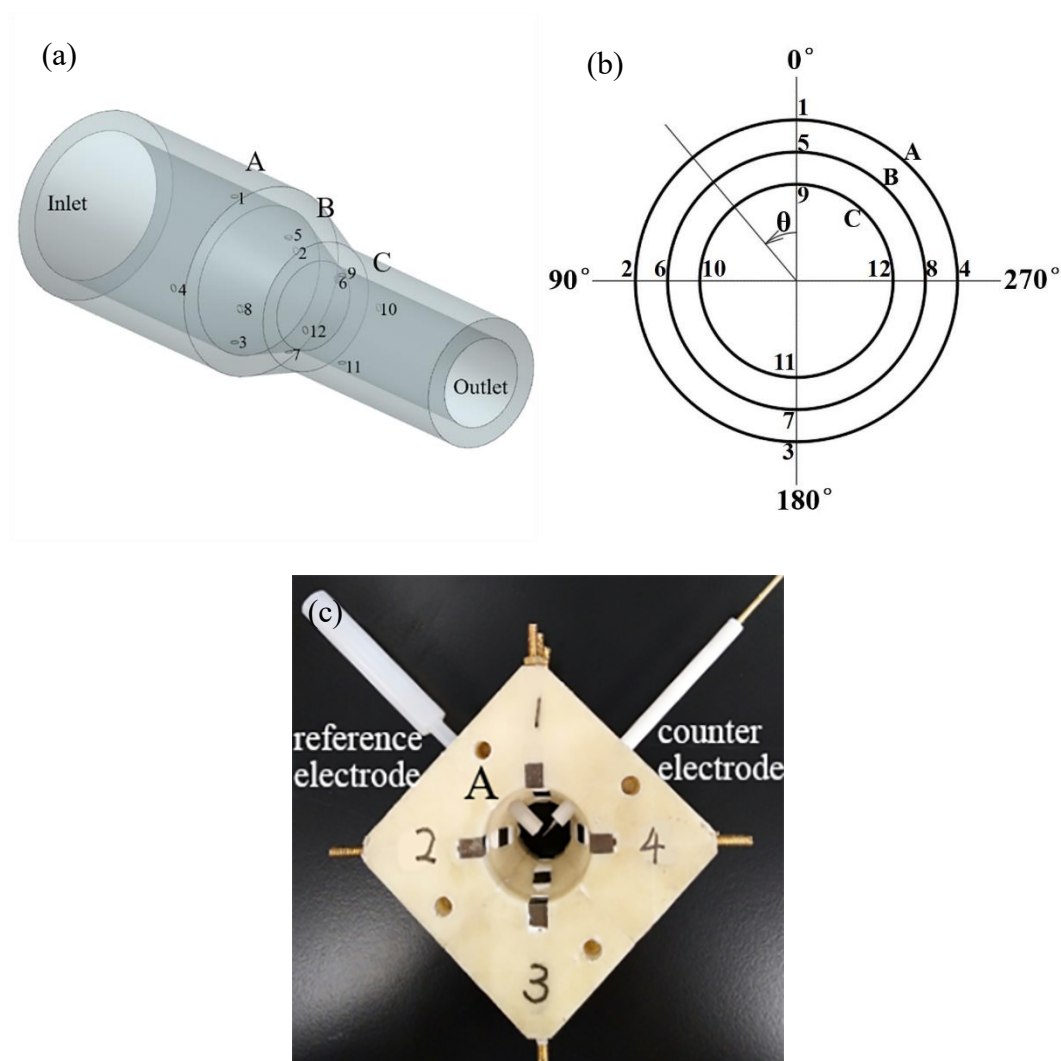
Figure 2. Electrode position diagram of the reducer, (a) complete picture, (b) annular angles θ, (c) assembly of the reducer test section and three-electrode system.

2.3 Electrochemical measurements

A three-electrode electrochemical cell was incorporated into the test section to perform *in situ* electrochemical measurements (Fig. 2c), in which the X65 steel specimen was used as working electrode (WE), a saturated calomel electrode (SCE) and a platinum plate were served as reference electrode (RE) and counter electrode (CE), respectively. The reducer test section was equipped with 12 electrodes. For purpose of shortening the test duration and minimize error caused by the long test time, electrochemical impedance spectroscopy (EIS) tests were conducted at a frequency range from 10,000 Hz to 0.1 Hz and an amplitude of 10 mV under open-circuit potential (OCP). The test duration of the 12 electrodes was 50 min. EIS measurements were performed after 3, 6 and 9 hours' erosion–corrosion tests. After EIS measurements, EIS spectrum of all electrodes were analyzed by ZSimpWin software with appropriate equivalent.

The corrosion rate (V_C) was derived by Stern–Geary equation $i = \frac{B}{R_{ct}}$ and Faraday's law $V_C = \frac{Mi}{nF} \times 10^4$ [14], as shown in the following equation (1):

$$V_C = \frac{MB}{nFR_{ct}} \times 10^4 \tag{1}$$

where V_C is the corrosion rate (g/(m² • h)), M is the atomic weight of metal (55.85), B is Stern–Geary constant, n is the number of electrons, F is the Faraday constant, R_{ct} is the charge transfer resistance calculated by ZSimpWin software, i is the current density (A/cm²). The corrosion rate was obtained by the average value of three times.

To obtain the value of B, the polarization curve of electrode A0° during erosion–corrosion test was determined at a scan rate of 1 mV/s. The corrosion potential (E_{corr}), current density (I_{corr}) and B were fitted and calculated.

2.4. Computational fluid dynamic simulation

The numerical simulations of erosion–corrosion behavior were analyzed by Fluent computational fluid dynamics software. A two-way coupled Eulerian-Lagrangian approach was utilized to investigate the erosion of reducer liquid-solid flow. The fluid was regarded as a continuous phase and sand particles as a discrete phase. The former was solved by the Navier-Stokes equations in Eulerian scheme and the latter was captured by discrete phase model (DPM) in Lagrangian framework. Corrosion was not considered in this simulation.

Geometric model was consistent with the actual pipe in the experiment. In order to achieve a fully developed flow and avoid backflow, the lengths of inlet and outlet straight pipe were 10 D_1 and 10 D_2, respectively. (D_1 and D_2 were the inner diameter of the large head and small head of reducer, respectively). The mesh used in the simulation was hexahedral cell, which guaranteed more stability and generated less diffusivity in the simulation. The liquid phase and solid phase were water and sand, respectively. The Reynolds number calculated from the geometrical dimension of tube and flow velocity was 14928, indicating fluid flow was a turbulent flow. Then, standard k-e two equation model was used to simulate the turbulent characteristics. And turbulent intensity was 4.8%, which was obtained from Reynolds number. Velocity inlet and outflow outlet were defined as the boundary conditions. The mass flow rate of the sand particles was 9.37 g/s, which was determined on the basis of flow velocity of inlet and sand loading 1 wt%. The convergent criteria were set as that residual in control volume for every equation was smaller than 0.00001 or the number of iterations reached to 6000.

Particle Erosion and Accretion model was used for the erosion model. The erosion rate of the reducer was achieved from the following formula [24]:

$$R_{erosion} = \sum_{p=1}^{N_{particles}} \frac{\dot{m}_p C(d_p) f(\alpha) v^{b(v)}}{A_{face}} \tag{2}$$

where $C(d_p)$ is a function of particle diameter, 1.8×10^{-9}, α is the impact angle of the particle path with the wall face, $f(\alpha)$ is a function of impact angle, v is the particle velocity, $b(v)$ is a function of particle velocity, 2.6, and A_{face} is the area.

3. RESULTS

3.1. Erosion behavior

Fig. 3 shows the distributions of velocity and sand particle concentration in the reducer. Clearly, when fluid flows through the reducer the outer fluid changes the direction of the flow field under the influence of the diameter reduction and flows at a corresponding angle to the side wall. In every part (Parts A, B and C), the velocity of tube top, side and bottom is approximately the same. The velocity of inlet straight pipe (Part A), reducer section (Part B) and outlet straight pipe (Part C) is 0.36, 0.70 and 1.38 m/s respectively, which indicating the velocity increases with the reduction of tube diameter. At the tube top, there is a lower sand particle concentration. However, under the influence of gravity, the sand particle concentration is increased at the location of tube bottom. Moreover, the particle concentration increases with the reduction of pipe diameter.
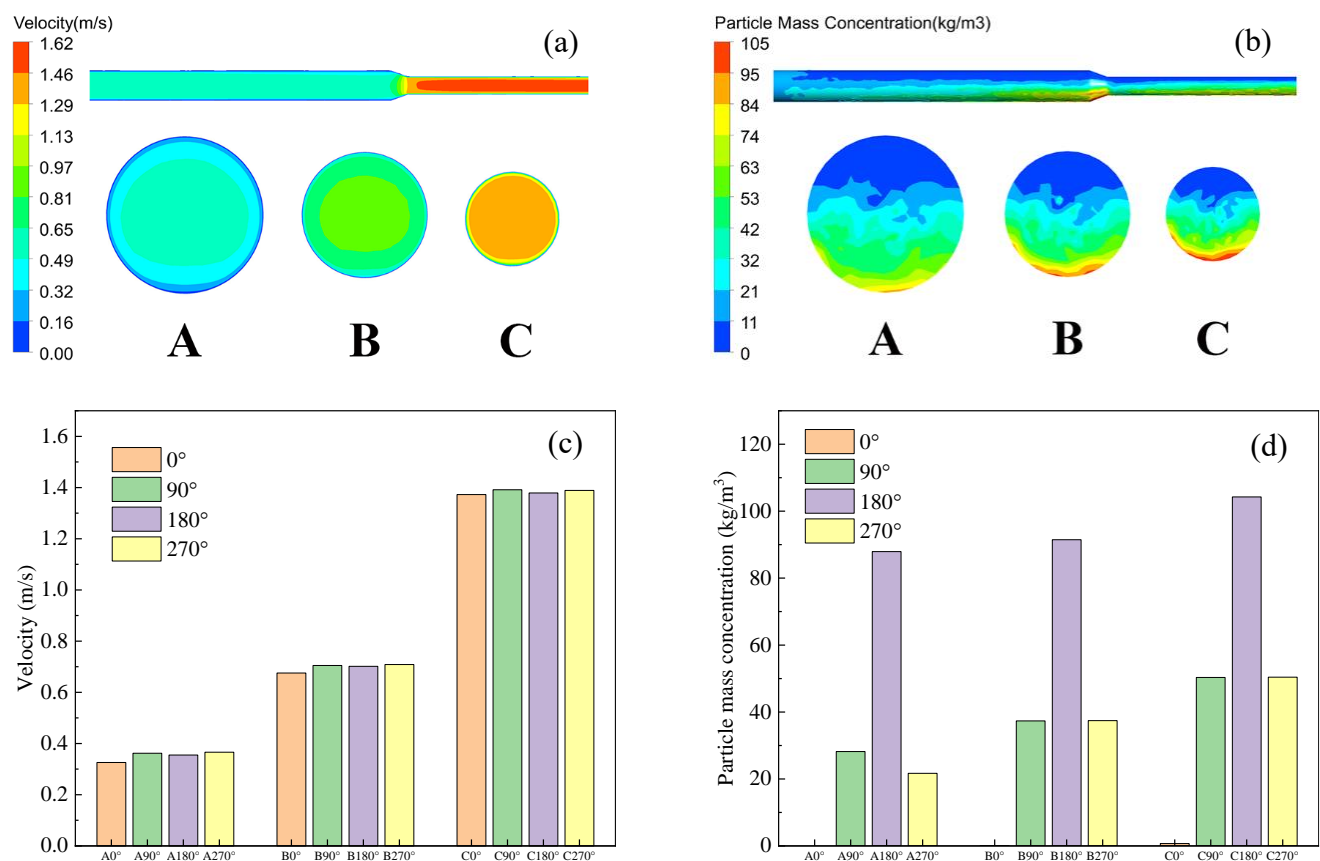

Figure 3. Distributions of velocity and particle mass concentration at a flow velocity of 0.5 m/s and a sand particle concentration of 1wt% in the reducer, (a) contour of velocity magnitude, (b) contour of sand particle concentration, (c) distribution of velocity at the reducer test part, (d) distribution of sand particle concentration at the reducer test part.
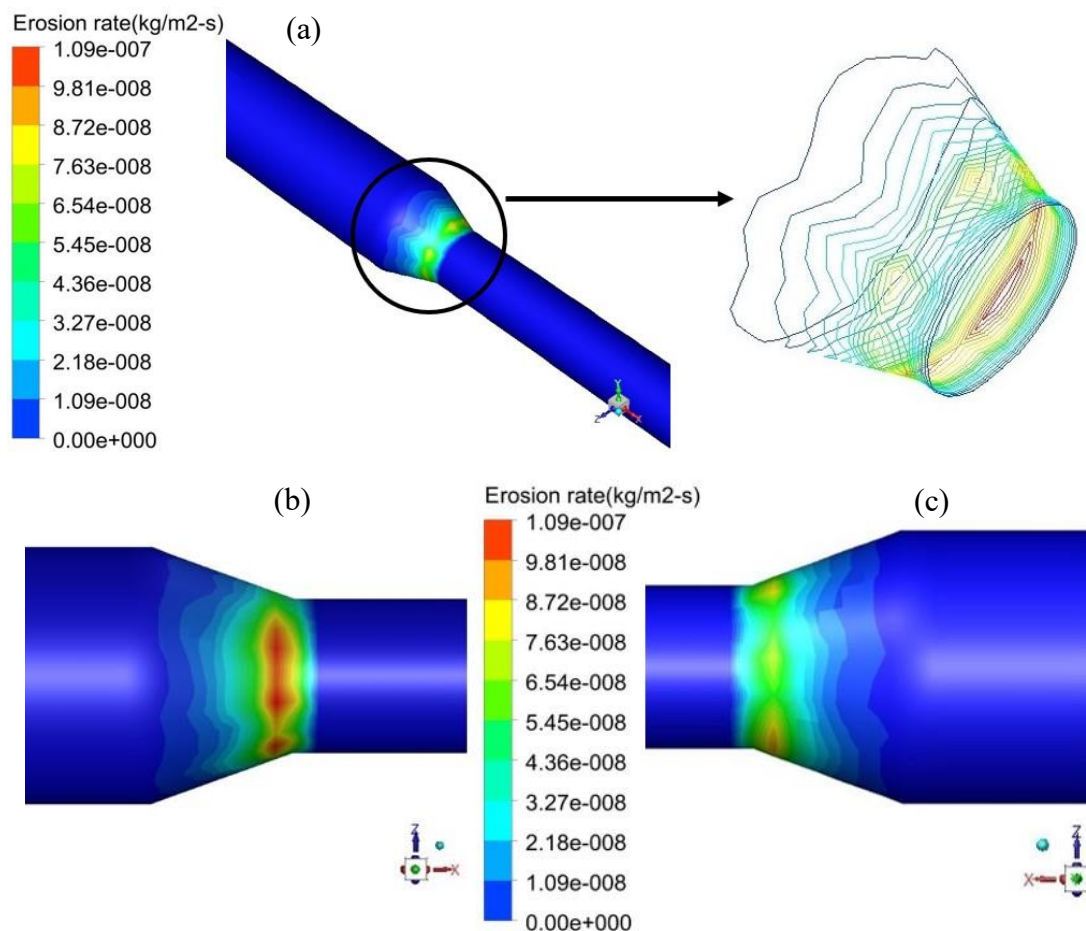
Figure 4. CFD results of erosion rate (kg/m^2·s) at a flow velocity of 0.5 m/s and a sand particle concentration of 1wt% in the reducer, (a) contours of erosion rate, (b) at the tube bottom, (c) at the tube top.

The erosion distributions of reducer are shown in Fig. 4. Remarkably, the erosion rate increases with the reduction of tube diameter and with the increase of annular angle θ (from top, side to bottom of pipe). As fluid flows from large head to small head, the flow velocity increases and particle concentration is high due to the decreasing of pipe diameter. The velocity of the particles increases with the fluid velocity, which causing the energy and frequency of particle collision with the wall surface also increase. The number of particles hitting the unit wall increases due to high particle concentration. Therefore, the maximum erosion rate is located at the tube bottom of reducer outlet. The differences in velocity and sand concentration cause the differences in erosion rates at different positions of the reducer.

3.2. Corrosion rate

Fig. 5 is the Nyquist plots of 12 electrodes after 6 h erosion–corrosion test. In all these Nyquist plots, there is a depressed semicircle over the whole frequency range. The diameter of the depressed semicircle reduces with the decreasing of pipe diameter (from Part A, Part B to Part C). This phenomenon indicates a small corrosion rate in inlet straight pipe (Part A) but a large corrosion rate in outlet straight pipe (Part C). The diameter of the depressed semicircle reduces with the increase of angle

θ (from tube top, tube side to tube bottom). This condition demonstrates a small corrosion rate at the top of pipe but a large corrosion rate at the bottom of pipe.
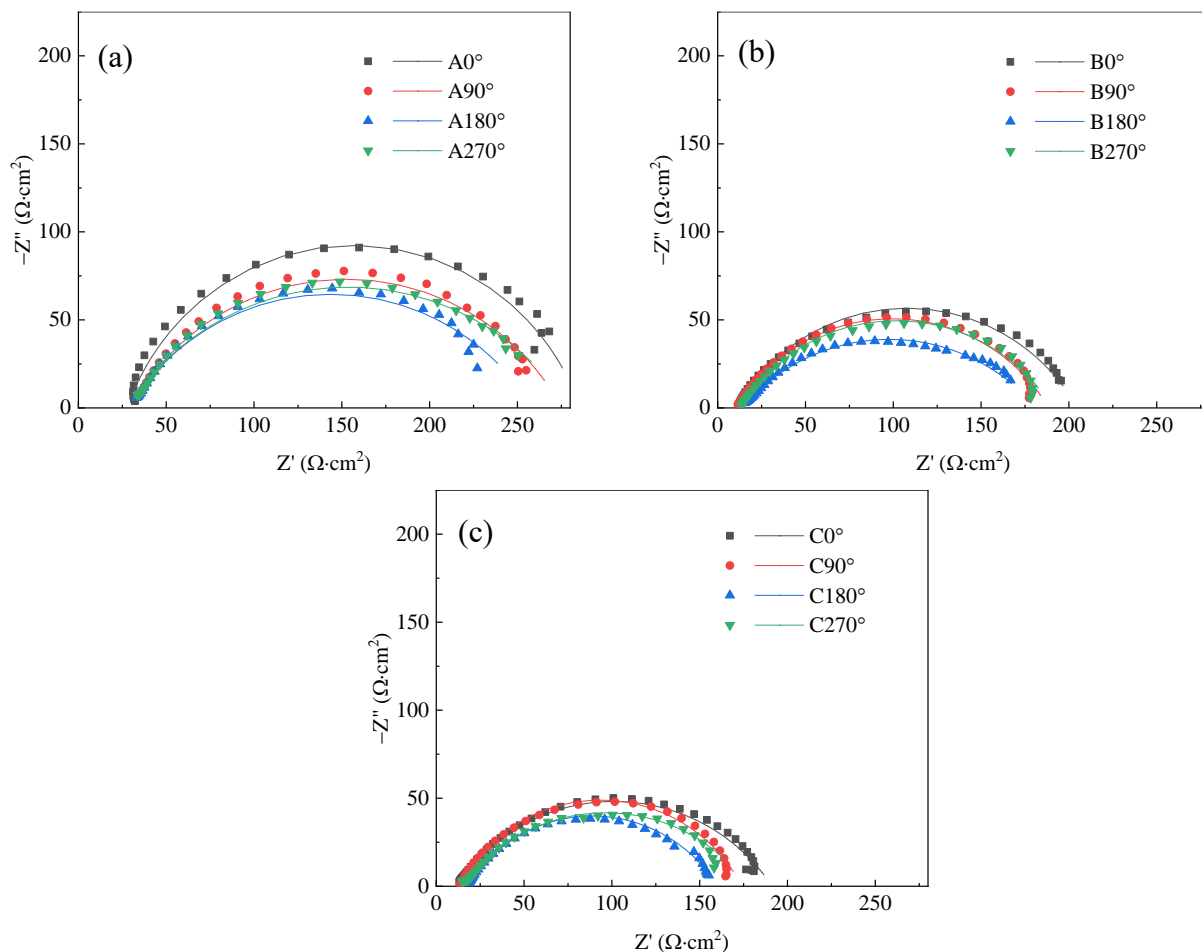

Figure 5. Nyquist plots of X65 steel electrodes after 6 h erosion–corrosion test in oilfield formation water, (a) in inlet straight pipe, (b) at the reducer section, (c) in outlet straight pipe. (the black curve is 0°, the red curve is 90°, the blue curve is 180°, the green curve is 270°)

To analyze the impedance spectroscopy parameters, equivalent circuit shown in Fig. 6 was applied to analyze EIS spectrum. R_s is the solution resistance, R_{ct} is the charge transfer resistance and Q_{dl} is the double layer capacitance. The fitting results of parameters are displayed in Table 2.

Fig. 7 shows the change of R_{ct} at the different locations of reducer. At the bottom of pipe, R_{ct} is 230.1 $\Omega \cdot cm^2$, 167.8 $\Omega \cdot cm^2$ and 142.8 $\Omega \cdot cm^2$ in inlet straight pipe (Part A), reducer section (Part B) and outlet straight pipe (Part C) respectively. This reveals that R_{ct} decreases with the reduction of tube diameter. In inlet straight pipe, R_{ct} is 257.9 $\Omega \cdot cm^2$, 245.2 $\Omega \cdot cm^2$ and 230.1 $\Omega \cdot cm^2$ at the position of tube top (θ=0º), side (θ=90º) and bottom (θ=180º) respectively. This result means that R_{ct} decreases with the increase of angle θ. The evolution of R_{ct} further indicates that the corrosion rate changes at the different locations of reducer.

Fig. 8 is the polarization curves of electrode A0º during erosion-corrosion test. The corrosion potential (E_{corr}), current density (I_{corr}) and B were calculated and shown in Table 3. From Table 3, it can be seen that constant B is calculated by the value of 20 mV/dec. According to the equation (1), corrosion rate can be obtained.
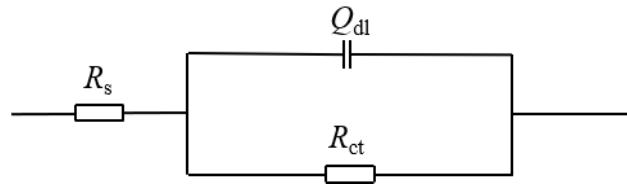
Figure 6. Equivalent circuit model served for EIS spectrum in Fig.6.

Table 2. Electrochemical parameters fitted from EIS spectrum in Fig.6.

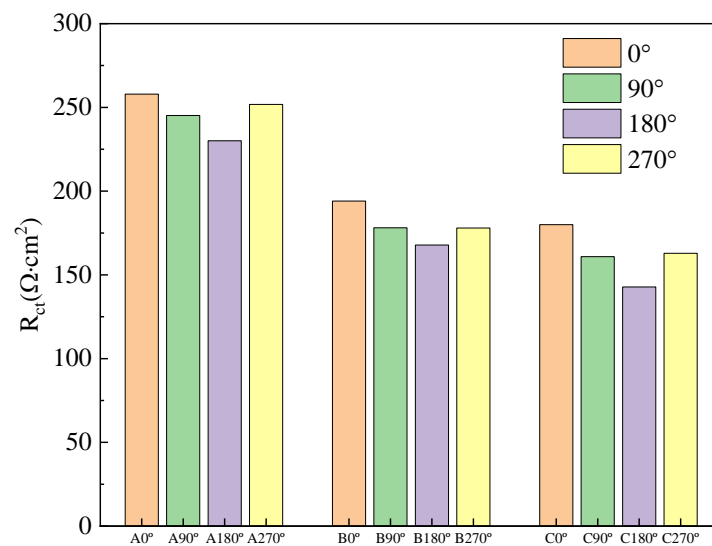| Electrode	R_S ($\Omega \cdot cm^2$)	Q_{dl} ($\mu F \cdot cm^{-2}$)	n	R_{ct} ($\Omega \cdot cm^2$)
A0º	27.90	447.7	0.7911	257.9
A90º	29.32	362.1	0.6848	245.2
A180º	28.60	752.0	0.6510	230.1
A270º	27.57	651.9	0.6358	251.8
B0º	10.71	469.4	0.6725	194.1
B90º	10.41	317.4	0.6591	178.1
B180º	13.76	848.9	0.5536	167.8
B270º	12.72	521.1	0.6477	178.0
C0º	9.93	506.1	0.6726	180.0
C90º	13.13	452.9	0.6970	160.9
C180º	17.37	480.6	0.6495	142.8
C270º	15.00	974.3	0.6038	162.9

Figure 7. Variation of R_{ct} of X65 steel electrodes with the position of electrode at the reducer test section after 6 hours erosion–corrosion test in oilfield formation water. (the orange column is 0°, the green column is 90°, the purple column is 180°, the yellow column is 270°)

3.3. Erosion–corrosion rate (V_T)

Fig. 9 is the distributions of total erosion–corrosion rate (V_T) of electrodes at the reducer test section. At the bottom of pipe, erosion–corrosion rates of inlet straight pipe (Part A), reducer section (Part B) and outlet straight pipe (Part C) are 1.6, 2.4 and 3.4 g/(m² • h), respectively. Notably, total erosion–corrosion rate increases with the reduction of pipe diameter (from Part A, Part B to Part C). In inlet straight pipe, the erosion–corrosion rates of tube top ($\theta=0°$), side ($\theta=90°$) and bottom ($\theta=180°$) are 1.3, 1.4 and 1.6 g/(m² • h), respectively. The total erosion–corrosion rate increases with the increase of angle θ. Therefore, the maximum erosion–corrosion rate occurs at the bottom of outlet straight pipe (C180°).
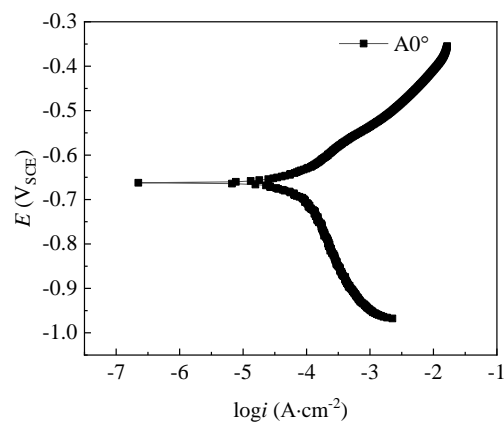

Figure 8. Polarization curve of electrode A0º during erosion–corrosion test in oilfield formation water.

Table 3. Polarization curve parameters of electrode A0º during erosion–corrosion test in oilfield formation water.

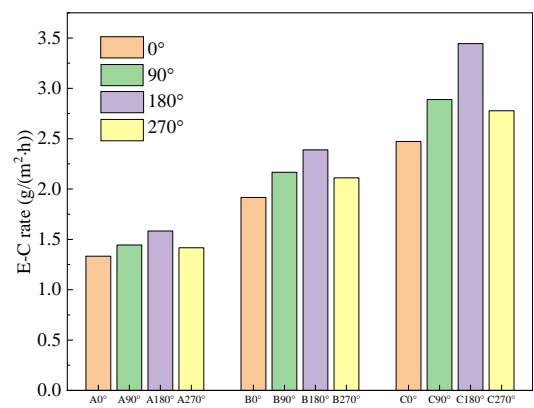| Electrode	E_{corr} (V_{SCE})	I_{corr} (A/cm²)	b_a (mV/ dec)	b_c (mV/ dec)	B (mV/dec)
A0º	-0.662	7.34×10^{-5}	60	198	20

Figure 9. Distribution of total erosion–corrosion rate (V_T) of all X65 steel electrodes at the reducer test part. (the orange column is 0°, the green column is 90°, the purple column is 180°, the yellow column is 270°)

3.4. Corroded morphology

Fig. 10 shows SEM images of representative electrodes after 12 hours' erosion–corrosion test. In the inlet straight pipe, the corrosion products formed on the tube top (electrode A0º) in Fig.10a are more compact than those at the tube side (electrode A90º) in Fig.10b and tube bottom (electrode A180º) in Fig.10c. Moreover, the porosity of electrode surface increases with the increase of angle θ (from tube top, tube side to tube bottom). At the tube bottom, the corrosion products in the inlet straight pipe (electrode A180º) in Fig.10c are more compact than those at the reducer section (electrode B180º) in Fig.10d and in the outlet straight pipe (electrode C180º) in Fig.10e, and the porosity of electrode surface increases with the reduction of pipe diameter.
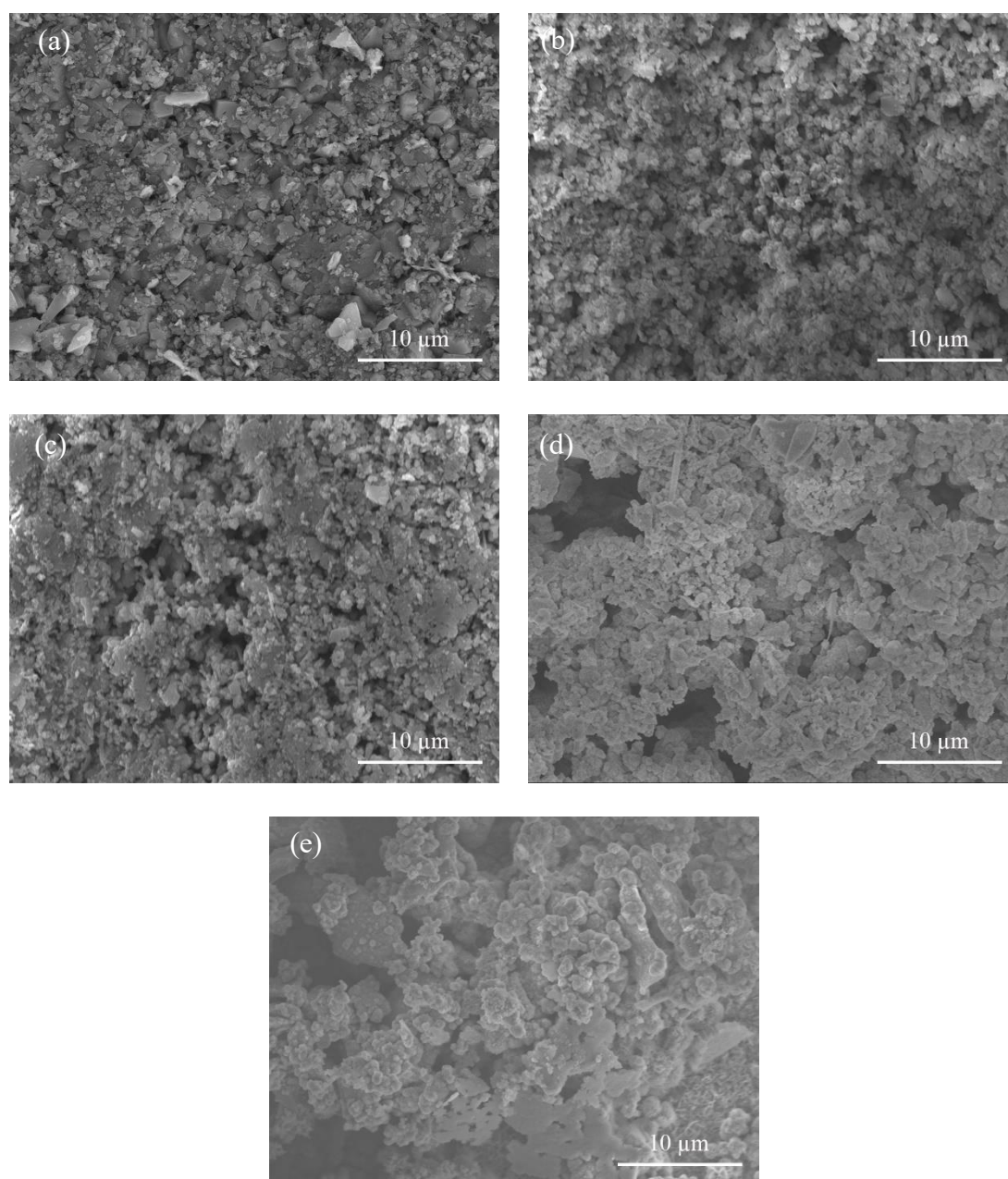

Figure 10. SEM morphologies of representative electrodes after erosion–corrosion experiment in oilfield formation water, (a) electrode A0º, (b) A90º, (c) A180º, (d) B180º and (e) C180º.

Fig. 11 shows SEM morphologies of representative electrodes after removing corrosion products. It can be seen that the surface morphologies of erosion–corrosion are mainly composed by pits and grooves. Due to the effect of solid–liquid flow shear forces, corrosion pits mainly develop along the flow direction and corrosion grooves. In the inlet straight pipe, there are several corrosion pits at the tube top (electrode A0º) in Fig.11a. At the tube side (electrode A90º), the number of corrosion pits are increased and corrosion grooves are begun to form (Fig.11b). At the tube bottom (electrode A180º), there are much more grooves formed (Fig.11c).
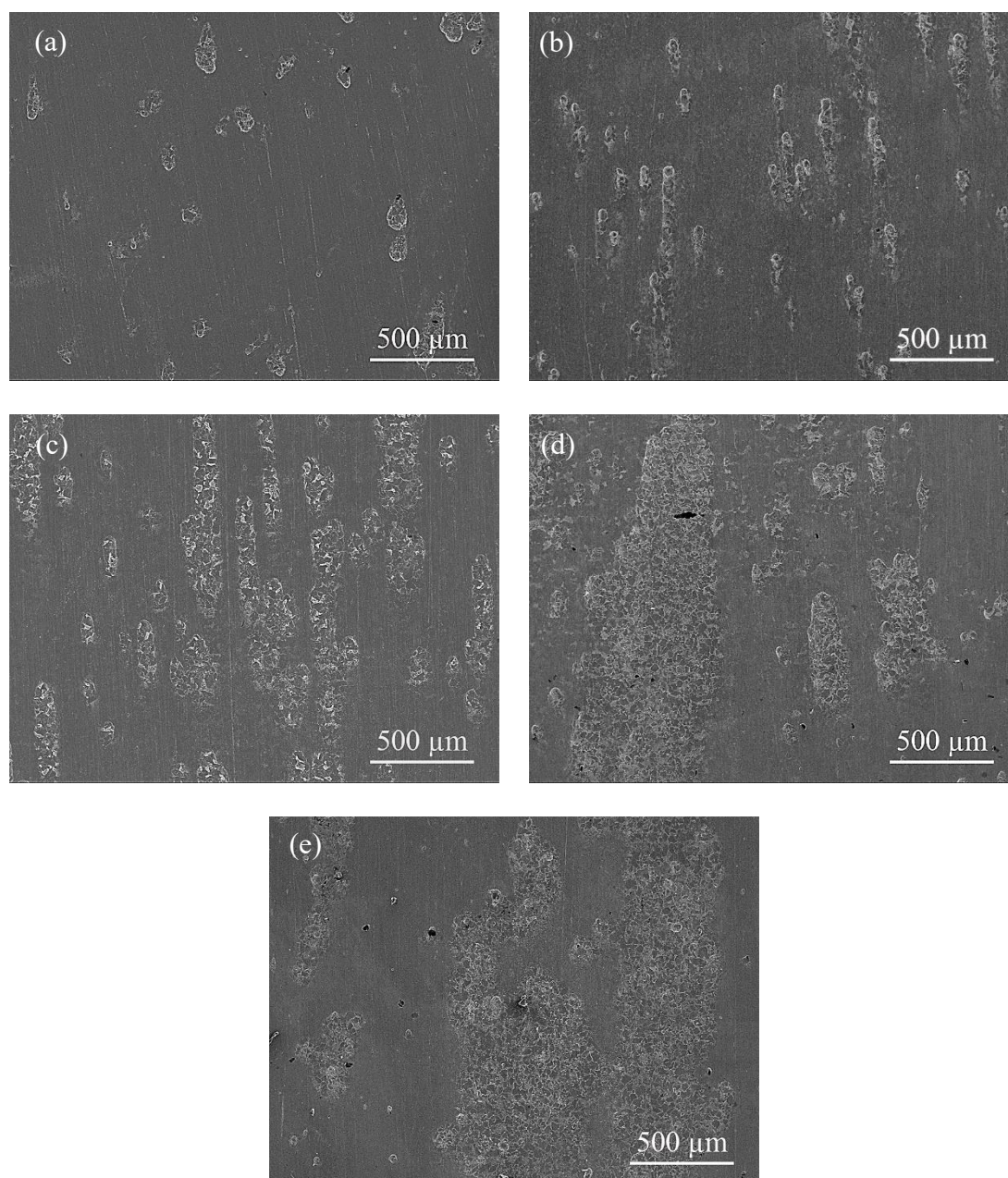

Figure 11. SEM morphologies of representative electrodes after removing corrosion products, (a) electrode A0º, (b) A90º, (c) A180º, (d) B180º and (e) C180º.

Along the flow direction of reducer (from electrode A180º, electrode B180º to electrode C180º), the areas of corrosion grooves are increased with the reduction of pipe diameter, and the largest corrosion

pits and grooves appears at the tube bottom of outlet straight pipe (electrode C180º) in Fig.11e. This highest erosion–corrosion rate at the bottom of outlet straight pipe is result from the mechanical effect between solid and liquid in the water flow [25].

4. DISCUSSION

4.1 Synergy of erosion and corrosion

In order to reveal the mechanism of erosion–corrosion, the synergistic effect of erosion and corrosion must be quantified. The erosion–corrosion rate can be calculated from the following formula [14, 26]:

$$V_T = V_C + V_E \tag{3}$$
$$V_T = V_{C0} + V_{E0} + \triangle V_C + \triangle V_E \tag{4}$$

where V_T is the total erosion–corrosion rate, V_C is the total corrosion rate, V_E is the total erosion rate, V_{C0} is the pure corrosion rate, V_{E0} is the pure erosion rate, $\triangle V_C$ is the erosion-enhanced corrosion rate, $\triangle V_E$ is the corrosion-enhanced erosion rate.

In this work, total erosion–corrosion rate (V_T) is obtained by weight loss measured before and after erosion–corrosion experiments; total corrosion rate (V_C) is determined by EIS measurements during the erosion–corrosion experiments; total erosion rate (V_E) is calculated by V_T - V_C; pure corrosion test is performed under static condition and pure corrosion rate (V_{C0}) is obtained by the weight loss measurements after 12 h corrosion tests; pure erosion rate (V_{E0}) is determined by weight loss measurement by applying a method of cathodic protection (-0.9 V vs. SCE) during erosion–corrosion tests; erosion-enhanced corrosion rate ($\triangle V_C$) is determined by V_C - V_{C0}; corrosion-enhanced erosion rate ($\triangle V_E$) can be calculated by V_E - V_{E0}.

The distribution of V_C and V_E of electrodes at the reducer test part are shown in Fig. 12a. In the inlet straight pipe, total corrosion rate is from 0.81 to 0.91g/(m^2 • h) and total erosion rate is from 0.53 to 0.68 g/(m^2 • h). In the outlet straight pipe, total corrosion rate is from 1.16 to 1.46 g/(m^2 • h) and total erosion rate is from 1.31 to 1.99 g/(m^2 • h). It can be seen that total corrosion rate (V_C) and total erosion rate (V_E) increase with the reduction of pipe diameter and the increase of the angle θ. Moreover, the total corrosion rate (V_C) is higher than total erosion rate (V_E) in the inlet straight pipe (Part A). However, total erosion rate (V_E) is higher than total corrosion rate (V_C) in the outlet straight pipe (Part C), with the opposite tendency of inlet straight pipe. This is because flow velocity and sand particle concentration increase with the decreasing of pipe diameter. Fig. 12 b and Fig.12 c show the percentages of V_C and V_E accounting for the total erosion–corrosion rate (V_T), respectively. It can be observed that the percentage of total corrosion rate (V_C) decreases with the reduction of pipe diameter and the increase of the angle θ. However, the variation tendency of the percentages of total erosion rate (V_E) is opposite to the trend of total corrosion rate.

Fig. 13 shows the distribution of the individual components (V_{C0}, V_{E0}, $\triangle V_C$ and $\triangle V_E$) of total erosion–corrosion rate and their percentages accounting for total erosion–corrosion rate. From Fig. 13 a, the pure corrosion rates (V_{C0}) at different positions are equal because it is obtained under static condition. V_{E0} is from 0.28 to 1.67 g/(m^2 • h), $\triangle V_C$ is from 0.68 to 1.36 g/(m^2 • h) and $\triangle V_E$ is from 0.12 to 0.51 g/(m^2 • h). Moreover, V_{E0} and $\triangle V_C$ increase with the reduction of pipe diameter and the increase of angle θ. $\triangle V_E$ increases with the reduction of pipe diameter and decreases with the increase of angle θ. Fig. 13e

to Fig.13h show the variation of percentages of these individual components accounting for total erosion–corrosion rate. The percentages of V_{C0} and $\triangle V_C$ are from 3.7% to 9.6% and from 39.6% to 51.0%, respectively, and their percentages decrease with the reduction of pipe diameter and the increase of angle θ. The percentage of $\triangle V_E$, from 8.3% to 20.6%, decreases with the increase of angle θ. However, the percentage of pure erosion (V_{E0}), from 20.8% to 48.4%, increases with the reduction of pipe diameter and the increase of angle θ. Furthermore, V_{E0} and $\triangle V_C$ have a great contribution to total erosion–corrosion rate while V_{C0} and $\triangle V_E$ have little contribution to total erosion–corrosion rate. Zeng [14] studied the erosion-corrosion of X65 carbon steel elbow and found that the pure erosion and erosion–enhanced corrosion account for large percentage of total erosion-corrosion rate while pure corrosion and corrosion–enhanced erosion account for small percentage of total erosion-corrosion rate. This was almost identical with the results in this investigation.
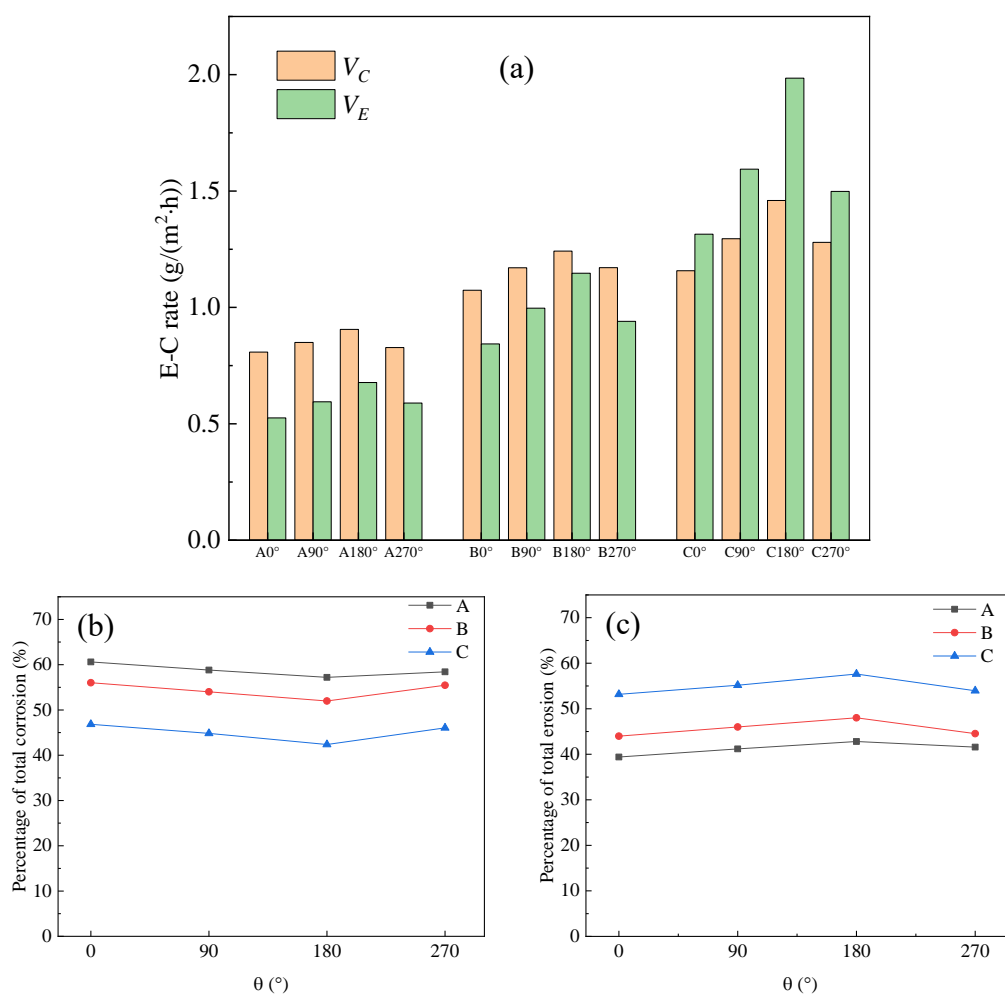

Figure 12. Distribution of V_C, V_E and variation of percentage of V_C, V_E accounting for V_T of all X65 steel electrodes at the reducer test section, (a) distribution of V_C, V_E, (b) variation of percentage of V_C accounting for V_T, (c) variation of percentage of V_E accounting for V_T.
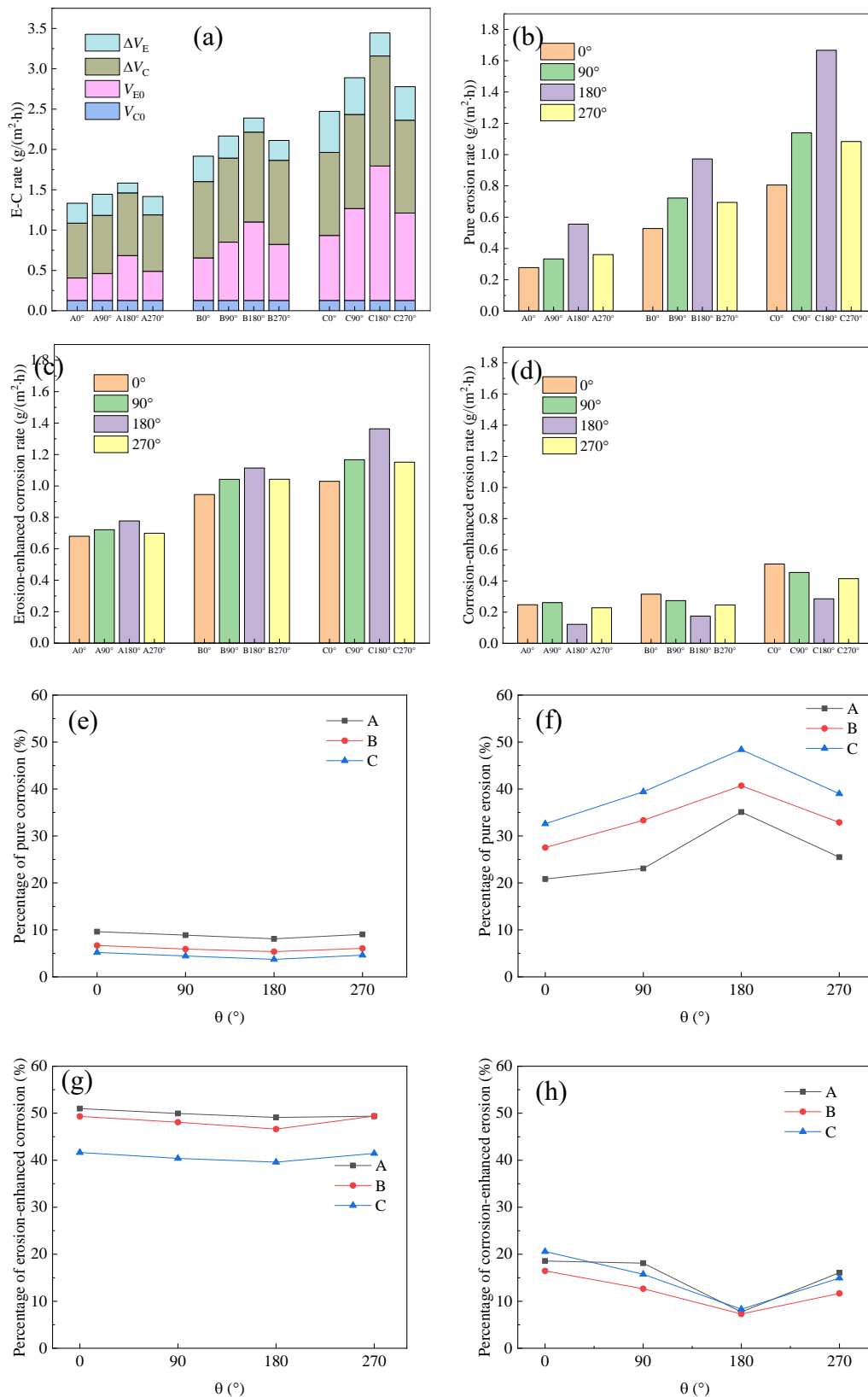
Figure 13. Distribution of four components of total erosion–corrosion rate and their percentages accounting for V_T of all X65 steel electrodes at the reducer test section, (a) distribution of four components, (b) distribution of V_{E0}, (c) distribution of $\triangle V_C$, (d) distribution of $\triangle V_E$, (e) variation of percentage of V_{C0}, (f) variation of percentage of V_{E0}, (g) variation of percentage of $\triangle V_C$, (h) variation of percentage of $\triangle V_E$.

4.2. Damage rules of reducer

From the above results, it can be concluded that there is a significant difference in the erosion–corrosion behavior at different positions of the reducer. Total erosion–corrosion rate increases with the reduction of pipe diameter and the increase of angle θ (from top, side to bottom of pipe). From the inlet straight pipe, reducer section to outlet straight pipe, the flow velocity increases (Fig. 4). The erosion–corrosion rate increases with the increase of flow velocity. The reason is that the increase of flow velocity accelerates the mass transfer process of oxygen, making it easy for oxygen to reach the surface of the sample and combine with the electrons to depolarize. Thus, steel corrosion is accelerated [16]. Zheng [27] reported that in flowing condition, the protective oxide film of metal is disrupted, which results in the increase of oxygen and the acceleration of corrosion. This is similar to the results of our research. At the same time, the kinetic energy of the sand particles and the number of sand particle impact per unit time increase with the increase of velocity, resulting in severe damage on the sample surface [28]. Therefore, the total erosion–corrosion rate increases with the reduction of pipe diameter. Liu [25] studied erosion–corrosion behavior of 90-degreee elbow at the flow velocity of 2.5, 3.5 and 4m/s and reported that the erosion–corrosion rates of all specimens tested increased with particle velocity within a certain range. The results were almost identical with the results obtained in this investigation.

The sand particle concentration at the tube bottom is higher than that at the tube top under the influence of gravity. During the erosion–corrosion test, the frequency of sand particles impacting the sample surface is high at the bottom of reducer due to the high sand particle concentration. The impact of solid particles causes the oxide film on the surface of the sample to fall off. Thus, the steel substrate comes in good contact with the corrosive species, making the corrosion more likely to occur [14]. Therefore, the total erosion–corrosion rate increases with the increase of angle θ. Islam [29] reported that erosion removes the corrosion film from the surface, breaks the cementite network, provides favorable conditions for pitting and increases the effective surface area by increasing the surface roughness. This is similar to the results of our research.

5. CONCLUSIONS

(1) The total erosion–corrosion rate increases with the decreasing of the reducer tube diameter. The total erosion–corrosion rate at the tube bottom is higher than that at the tube top. The total corrosion rate and total erosion rate increase with the decreasing of tube diameter and the increase of angle θ.

(2) The flow velocity increases along the reducer flow direction. The sand particle concentration at the reducer tube bottom is higher than that at the tube top. The erosion rate increases with the reduction of pipe diameter and the increase of angle θ.

(3) The pure erosion rate and erosion-enhanced corrosion rate have a great contribution to total erosion–corrosion rate, and the pure corrosion rate and corrosion-enhanced erosion rate have less contribution. The pure erosion rate and erosion-enhanced corrosion rate increase with the reduction of pipe diameter and the increase of angle θ. Corrosion-enhanced erosion rate increases with the reduction of pipe diameter and decreases with the increase of angle θ.

References

1. A. Neville and T. Hodgkiess, *Wear*, 233 (1999) 596.
2. W. Aperador, J. Caballero-Gomez and A. Delgado, *Int. J. Electrochem. Sci.*, 8 (2013) 6709.
3. Y. Wang, Z. Z. Xing, Q. Luo, A. Rahman, J. Jiao, S. J. Qu, Y. G. Zheng, J. Shen, *Corros. Sci.*, 98 (2015) 339.
4. M. M. Stack and G. H. Abdulrahman, *Wear*, 274 (2012) 401.
5. J. H. Xie, A. T. Alpas and D. O. Northwood, *J. Mater. Sci.*, 38 (2003) 4849.
6. S. Li, Y. Zuo and P. Ju, *Appl. Surf. Sci.*, 331 (2015) 200.
7. C. F. Dong, K. Xiao, X. G. Li and Y. F. Cheng, *Wear*, 270 (2010) 39.
8. Z. B. Zheng, Y. G. Zheng, W. H. Sun and J. Q. Wang, *Corros. Sci.*, 76 (2013) 337.
9. B. Poulson, *Wear*, 233 (1999) 497.
10. H. X. Guo, B. T. Lu, J. L. Luo, *Electrochim. Acta*, 51 (2005) 315.
11. N. Khayatan, H. M. Ghasemi, M. Abedini, *Wear*, 380-381 (2017) 154.
12. B. T. Lu, J. F. Lu, J. L. Luo, *Corros. Sci.*, 53 (2011) 1000.
13. R. C. Barik, J. A. Wharton, R. J. K. Wood, K. R. Stokes, *Wear*, 267 (2009) 1900.
14. L. Zeng, G. A. Zhang, X. P. Guo, *Corros. Sci.*, 85 (2014) 318.
15. M. A. Islam, Z. N. Farhat, E. M. Ahmed, A. M. Alfantazi, *Wear*, 302 (2013) 1592.
16. M. A. Islam, Z. N. Farhat, *Tribol. Int.*, 68 (2013) 26.
17. W. S. Peng, X. W. Cao, *Powder Technol.*, 294 (2016) 266.
18. I. Finnie, *Wear*, 3 (1960), 87.
19. Y. I. Oka, K. Okamura and T. Yoshida, *Wear*, 259 (2005) 95.
20. M. M. Stack, S. M. Abdelrahman, *Wear*, 273 (2011) 38.
21. K. Wang, X. Li, Y. Wang, R. He, *Powder Technol.*, 314 (2017) 490.
22. X. H. Chen, B. S. McLaury, S. A. Shirazi, *Comput. Fluids*, 33 (2004) 1251.
23. H. Jin, X. Chen, Z. Zheng, G. Ou, W. Liu, *Eng. Fail. Anal.*, 73 (2017) 46.
24. A. Campos-Amezcua, A. Gallegos-Munoz, C.A. Romero, Z. Mazur-Czerwiec, R. Campos-Amezcua, *Appl. Therm. Eng.*, 27 (2007) 2394.
25. J. Liu, W. BaKeDaShi, Z. Li, Y. Xu, W. Ji, C. Zhang, G. Cui, R. Zhang, *Wear*, 376 (2017) 516.
26. X. Tang, L.Y. Xu, Y. F. Cheng, *Corros. Sci.*, 50 (2008) 1469.
27. Q. Zheng, L. Zhang, X. Jie, X. Huang and S. Luo, *Int. J. Electrochem. Sci.*, 12 (2017) 2593.
28. Y. Yang and Y. F. Cheng, *Wear*, 276 (2012) 141.
29. M. A. Islam and Z. Farhat, *Wear*, 376 (2017) 533.